

# Cuprous oxide/copper oxide interpenetrated into ordered mesoporous cellulose-based carbon aerogels for efficient photocatalytic degradation of methylene blue

Rui Cui, Dongnv Jin, Gaojie Jiao, Zhendong Liu, Jiliang Ma (✉), Runcang Sun (✉)

Liaoning Key Lab of Lignocellulose Chemistry and Biomaterials, Liaoning Collaborative Innovation Center for Lignocellulosic Biorefinery, College of Light Industry and Chemical Engineering, Dalian Polytechnic University, Dalian 116034, China

© Higher Education Press 2023

**Abstract** The casual discharge of dyes from industrial settings has seriously polluted global water systems. Owing to the abundance of biomass resources, preparing photocatalysts for photocatalytic degradation of dyes is significant; however, it still remains challenging. In this work, a cuprous oxide/copper oxide composite was interpenetrated onto carbon nanosheets of cellulose-based flexible carbon aerogels ( $\text{Cu}_2\text{O}/\text{CuO}@CA_x$ ) via a simple freeze-drying-calcination method. The introduction of the carbon aerogel effectively prevents the aggregation of the cuprous oxide/copper oxide composite. In addition,  $\text{Cu}_2\text{O}/\text{CuO}@CA_{0.2}$  has a larger specific surface area, stronger charge transfer capacity, and lower recombination rate of photogenerated carriers than copper oxide. Moreover,  $\text{Cu}_2\text{O}/\text{CuO}@CA_{0.2}$  exhibited high photocatalytic activity in decomposing methylene blue, with a degradation rate reaching up to 99.09% in 60 min. The active oxidation species in the photocatalytic degradation process were systematically investigated by electron spin resonance characterization and poisoning experiments, among which singlet oxygen played a major role. In conclusion, this work provides an effective method for preparing photocatalysts using biomass resources in combination with different metal oxides. It also promotes the development of photocatalytic degradation of dyes.

**Keywords** carbon aerogel, photocatalysis, dye degradation, biomass, cuprous oxide/copper oxide

## 1 Introduction

Rapid developments in industry and agriculture have

Received November 28, 2022; accepted January 15, 2023;  
online May 3, 2023

E-mails: jlma@dlpu.edu.cn (Ma J.), rcsun3@dlpu.edu.cn (Sun R.)

considerably improved the global economy and accelerated the development of society while detrimentally affecting the environment [1,2]. In particular, the discharge of dye wastewater on a global scale has resulted in the pollution of water bodies and the depletion of drinkable water, threatening the survival of humans, animals and plants [3]. Methylene blue, first synthesized by Heinrich Caro in 1800, has an aromatic heterocyclic structure with the molecular formula  $\text{C}_{16}\text{H}_{18}\text{N}_3\text{ClS}$  and is the most commonly used dye in the textile industry [4]. It is highly soluble in water, readily forms stable solutions with water at room temperature and is commonly used to dye cotton, silk and paper. In addition, methylene blue is often used as a bacterial stain and indicator [5] and has been further utilized in the medical field to treat bacterial malaria [6]. However, methylene blue is toxic, carcinogenic and mutagenic, with exposure to its low concentrations resulting in diarrhea, nausea and vomiting [7]. When methylene blue concentration reaches a certain level in water bodies around the globe, mass extinction of aquatic life may occur. Moreover, the presence of methylene blue in water results in the production of deep-colored by-products, which reduce sunlight transmittance through the water. Consequently, there is a decrease in the levels of dissolved oxygen in water, affecting the survival of aquatic organisms [8]. Therefore, eliminating such pollutants from water is vital for achieving sustainable industrial and agricultural development.

Currently, the typical methods used for dye treatment are physical (adsorption and membrane separation) [9], biological (phytoremediation and aerobic) [10] and chemical methods (electrochemical oxidation, chemical precipitation and advanced oxidation) [11]. Physical methods proceed via a simple reaction mechanism, are easy to operate, and do not cause secondary water pollution. The popular materials used in physical methods include activated carbon [12], bentonite [13] and nanofiber

membranes [14]. Although these materials are low cost and efficient, they have limited adsorption capacity and reusability. Biological methods use microorganisms to chemically react with pollutants, converting organic pollutants into harmless inorganic substances, thereby achieving water purification [15]. However, although biological methods consume low energy, do not produce secondary water pollution and require low investment, their high environmental pH and temperature requirements greatly limit their application [16]. Chemical methods are based on the chemical reactions between chemical reagents and dyes to produce precipitates or simple compounds or on the degradation of dyes by redox substances and using an external electric field. These methods are currently popular because they are simple, efficient and controllable. However, they also have many limitations, such as high costs, production of secondary pollutants and high energy consumption [11]. Therefore, it would be beneficial to develop a new environmentally friendly, pollution-free technology for treating dyes with low cost, high efficiency and low energy consumption.

Photocatalysis is a green technology with significant application prospects in the energy and environmental fields. It has been widely used in the synthesis of organic acids [17] and furfuryl alcohol [18], hydrogen generation [19] and carbon dioxide (CO<sub>2</sub>) reduction [20]. Photocatalysis is the most promising technology for eliminating organic pollutants from wastewater owing to its environmental friendliness, low energy consumption, low cost and reusability, especially for methylene blue degradation. The key to achieving this goal is to develop an efficient and economical photocatalyst. Numerous photocatalysts have been developed, such as metal-free semiconductors [21] and metal oxides/sulfides [22]. Copper oxide-based nanoparticles have been widely used in photocatalysis owing to their wide range of light absorption, antimicrobial properties, excellent electrical and thermal conductivities, and suitable optical bandgap [23]. Typically, copper oxide (CuO) is an indirect bandgap semiconductor with a bandgap of 1.7 eV and a carrier diffusion length of 200 nm [24]. However, pure CuO exhibits low photocatalytic degradation of organic dyes in practical applications due to photocorrosion and rapid recombination of photogenerated carriers. Due to the synergistic geometrical and electronic aspects or strain and ligand effects, nanocomposites composed of two metal oxides exhibit superior catalytic activity compared to single metal oxides [25]. The disadvantages of single-component CuO photocatalysts can be modified by combining with other components (e.g., cerium oxide, cuprous oxide, titanium dioxide, ferric oxide) [26–29]. As we know, Cu<sub>2</sub>O is a direct bandgap semiconductor with a bandgap of 2.2 eV and a carrier diffusion length of 500 nm. As a typical p-type semiconductor photocatalyst with a suitable band gap, low toxicity and a wide visible light absorption range, Cu<sub>2</sub>O has attracted a lot of

interest. Meanwhile, the photocatalytic performance of photocatalysts depends on the intrinsic carrier dynamics such as carrier mobility, life-time, diffusion length and density. Surprisingly, the carrier mobility of Cu<sub>2</sub>O is 30–130 cm<sup>2</sup>·V<sup>-1</sup>·s<sup>-1</sup>, which is significantly higher than that of other photocatalysts (e.g., titanium dioxide, bismuth vanadium oxide, ferric oxide, and tungsten trioxide) [30]. Moreover, some researches have shown that CuO and Cu<sub>2</sub>O can be interconverted, which avoids the addition of other functional materials, leading to the low production costs [31]. However, the nanocatalysts often suffered from aggregation/clumping due to the high surface energies of the particles, resulting in poor photocatalytic activity. Moreover, nanoscale catalysts are difficult to be recycled. Therefore, developing a new process for synthesizing highly active, stable and recyclable CuO/Cu<sub>2</sub>O-based photocatalysts is of great significance.

Carbon aerogels are recognized as excellent carrier materials for loaded heterogeneous catalysts owing to their high porosity, excellent electronic conductivity and physicochemical stability [32]. The materials commonly used for preparing carbon aerogels include graphene oxide [33], graphitic carbon nitride [34] and metal-organic frameworks [35]. However, the carbon precursors of these materials are mainly derived from non-renewable fossil resources, leading to the high cost. To this end, a more efficient and economical route to fabricate new carbon aerogels with high performance would be advantageous. The developments of biomass-based carbon aerogels with abundant renewable raw materials, low cost and environmental friendliness make them expected to be a sustainable alternative for non-renewable carbon materials [36]. Carboxymethylcellulose sodium (CMC) and cellulose nanofibers (CNFs) produced from decomposing plant cellulose are the most abundant and sustainable biopolymers on earth, which are ideal precursors for synthesizing biomass-based carbon aerogels. The obtained CMC/CNF-based carbon aerogels have low density, three-dimensional interconnected pores, high electrical conductivity and excellent adsorption capacity. Moreover, the CMC and CNF structures have natural compatibility, with the introduction of CNF giving CMC/CNF-based carbon aerogels excellent compressibility and elasticity [37]. While other biomass precursors used to prepare carbon aerogels include alginate [38], chitosan [39], and starch [40], the poor thermal stability of these biomass polymers results in the carbon aerogels prepared being fragile and incompressible [41], which greatly limits the practical application of them. Hence, the combination of heterogeneous catalysts with CMC/CNF-based carbon aerogels to prepare novel photocatalysts has great potential.

Herein, we report the interpenetration of a Cu<sub>2</sub>O/CuO composite into cellulose-based carbon nanosheets (named Cu<sub>2</sub>O/CuO@CA<sub>x</sub>) using a simple freeze-drying-calcination method for photocatalytic degradation of methylene

blue, where CuO nanobelt precursor was partly reduced to Cu<sub>2</sub>O. We carefully investigated the optimal reaction conditions for the photocatalytic degradation of methylene blue. In addition, the active oxidation species produced in the photocatalytic degradation of methylene blue were investigated by electron spin resonance (ESR) characterization and poisoning experiments. The possible reaction mechanism of the photocatalytic degradation methylene blue process was further elucidated. Overall, this study effectively combines biomass resources with different types of metal oxide nanomaterials, which shows great potential in treating dyes in wastewater.

## 2 Experimental

### 2.1 Preparation of CuO

First, 110.0 g of sodium hydroxide (NaOH) was slowly added to 0.9 L of deionized water. Following the complete dissolution of NaOH, 20.0 g of hexadecyl trimethyl ammonium bromide (CTAB) was slowly added in the obtained solution under magnetic stirring conditions. Subsequently, the mixed system was heated to 60 °C to obtain NaOH-CTAB solution. Additionally, 3.1 g of cupric nitrate was precisely weighed and dissolved in 0.1 L of deionized water. The obtained solution was injected into the NaOH-CTAB solution and stirred magnetically for 1 h. The system was then filtered at 60 °C, and the filter cake was washed with ethanol and deionized water to neutral. The black solid samples were dried in an open oven at 50 °C for 12 h. Finally, these dried black powders were further calcined under N<sub>2</sub> atmosphere (350 °C, 120 min) to obtain CuO.

### 2.2 Preparation of Cu<sub>2</sub>O/CuO@CA<sub>x</sub>

Different CuO dosages (0.1 g, 0.2 g and 0.3 g) were added to 20 mL of deionized water and dispersed adequately, respectively. Then, 1.0 g of CMC was dissolved into the above dispersion. After that, 1.0 g of CNF was slowly added, and the obtained solution was mechanically stirred for 120 min. The mixed samples were freeze-dried and then calcinated at 500 °C for 120 min under nitrogen atmosphere to obtain Cu<sub>2</sub>O/CuO@CA<sub>x</sub> (named as Cu<sub>2</sub>O/CuO@CA<sub>0.1</sub>, Cu<sub>2</sub>O/CuO@CA<sub>0.2</sub> and Cu<sub>2</sub>O/CuO@CA<sub>0.3</sub>, respectively).

### 2.3 Photocatalytic activity measurements

The photocatalytic properties of Cu<sub>2</sub>O/CuO@CA<sub>0.2</sub> were studied by degradation of methylene blue dye under the irradiation of a 300 W Xenon lamp. The influences of pH values on the photocatalytic degradation of methylene blue were first investigated. Specifically, methylene blue solutions (100 ppm) with pH values of 7, 8, 9, 10, and 11

were prepared and then 10 mg of Cu<sub>2</sub>O/CuO@CA<sub>0.2</sub> was added. The mixed system was first stirred at 500 r·min<sup>-1</sup> for 40 min under darkness to reach adsorption/desorption equilibrium. Then, the reaction was reacted for 60 min under the irradiation of visible light. The reacted solution was filtered through a microporous filter (0.22 μm) and the concentrations were measured with a ultraviolet-visible spectrophotometer at a wavelength of 664 nm. Under the optimal pH, the effects of Cu<sub>2</sub>O/CuO@CA<sub>0.2</sub> dosages, irradiation time and CuO addition in CuO/CuO@CA<sub>x</sub> on the photocatalytic degradation of methylene blue were also investigated. All the above reactions were carried out at room temperature.

The degradation efficiency of methylene blue was calculated by the following equation:

$$\text{Removal efficiency (\%)} = \frac{C_e - C_t}{C_e} \times 100\%,$$

where  $C_e$  (mg·L<sup>-1</sup>) and  $C_t$  (mg·L<sup>-1</sup>) represented the methylene blue concentrations before and after being degraded for a certain time, respectively.

## 3 Results and discussion

### 3.1 Catalyst synthesis and characterization

The preparation schematic, scanning electron microscopy (SEM) images, elemental mapping images and the energy-dispersive X-ray spectroscopy (EDS) of Cu<sub>2</sub>O/CuO@CA<sub>0.2</sub> are shown in Fig. 1. The preparation of Cu<sub>2</sub>O/CuO@CA<sub>x</sub> is illustrated in Fig. 1(a), mainly including directional freezing-casting, vacuum freeze-drying, and calcination strategies. First, CMC and CNF were used as carbon sources and dissolved in a dispersion of CuO nanobelt, followed by directional freezing-casting and vacuum freeze-drying to obtain Cu<sub>2</sub>O/CuO@CA<sub>x</sub> precursors. Lastly, a controllable calcination was carried out to acquire Cu<sub>2</sub>O/CuO@CA<sub>x</sub> with vertically aligned layered structure. The morphology of the prepared Cu<sub>2</sub>O/CuO@CA<sub>0.2</sub> was studied by SEM. It is apparent from the images in Figs. 1(b) and 1(c) that Cu<sub>2</sub>O/CuO@CA<sub>0.2</sub> exhibits a structure with vertically aligned layers; this structure ensures the stability and flexibility of the material. Figures 1(d) and 1(e) show the uniform distribution of interpenetrated Cu species into ordered mesoporous cellulose-based carbon aerogels. In addition, the elemental mapping images (Figs. 1(f)–1(i)) show a uniform distribution of C, N, O and Cu in the composites, indicating that the Cu species were successfully interpenetrated into the carbon nanosheets in carbon aerogels. Furthermore, EDS data (Fig. 1(j)) show C, N, O and Cu contents of 68.52, 0.10, 15.94 and 10.95 wt%, respectively.

Figure 2 shows the N<sub>2</sub> adsorption–desorption isotherms and Fourier transform infrared (FTIR) spectra of CuO and Cu<sub>2</sub>O/CuO@CA<sub>0.2</sub>. To better illustrate the interpenetra-

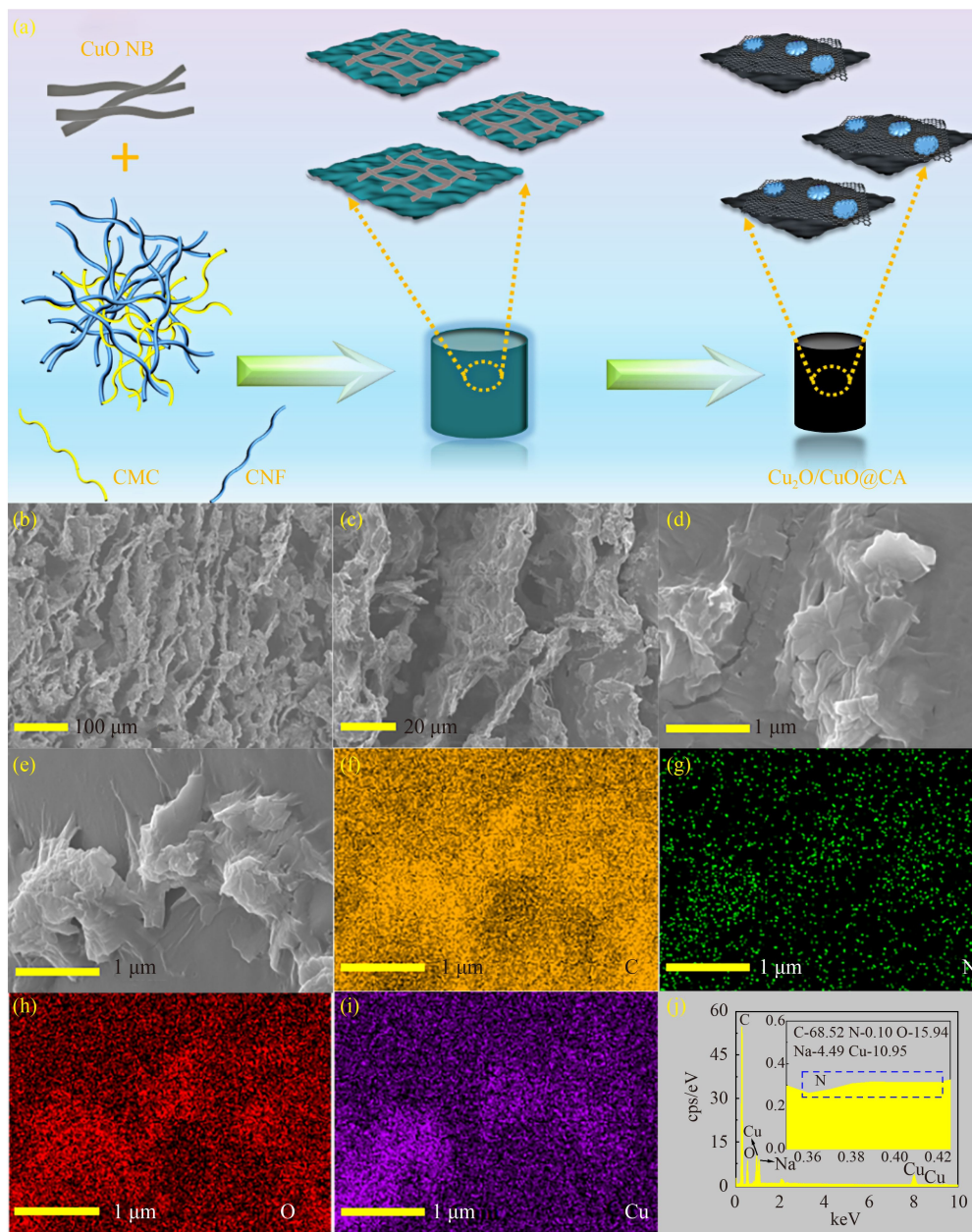


**Fig. 1** (a) Schematic of  $\text{Cu}_2\text{O}/\text{CuO}@CA_x$  preparation. (b–e) Scanning electron microscopy images of  $\text{Cu}_2\text{O}/\text{CuO}@CA_{0.2}$ . Elemental mapping images of  $\text{Cu}_2\text{O}/\text{CuO}@CA_{0.2}$ : (f) C, (g) N, (h) O and (i) Cu. (j) Energy-dispersive X-ray spectroscopy of  $\text{Cu}_2\text{O}/\text{CuO}@CA_{0.2}$ .

ting effect of  $\text{Cu}_2\text{O}/\text{CuO}$  into carbon nanosheets in case of carbon aerogels on the surface area and pore size distribution,  $\text{CuO}$  and  $\text{Cu}_2\text{O}/\text{CuO}@CA_{0.2}$  were subjected to  $\text{N}_2$  adsorption–desorption measurements. As shown in Fig. 2(a), both materials exhibit IV-type isotherms, indicating an abundance of mesopores in their structures (Fig. 2(b)). Moreover, the specific surface area of  $\text{Cu}_2\text{O}/\text{CuO}@CA_{0.2}$  ( $26.71 \text{ m}^2 \cdot \text{g}^{-1}$ ) was considerably higher than  $\text{CuO}$  ( $7.79 \text{ m}^2 \cdot \text{g}^{-1}$ ). This phenomenon can be attributed to the combination of a  $\text{Cu}_2\text{O}/\text{CuO}$  compound with a carbon aerogel exhibiting a layered structure, which is consistent with the SEM results. Meanwhile, the higher specific

surface area of  $\text{Cu}_2\text{O}/\text{CuO}@CA_{0.2}$  compared to  $\text{CuO}$  may enhance the adsorption and mass transfer properties of the photocatalyst, improving its photocatalytic efficiency.

To investigate the Cu species on the prepared materials, the functional groups on the material's surface were investigated using FTIR spectroscopy. As shown in Fig. 2(c), the characteristic absorption band at  $3442 \text{ cm}^{-1}$  is attributed to the stretching vibration of O–H. The characteristic peak at  $494 \text{ cm}^{-1}$  in the FTIR spectrum of  $\text{CuO}$  is because of the bending vibration of Cu–O [42]. The band at  $672 \text{ cm}^{-1}$  in the FTIR spectrum of  $\text{Cu}_2\text{O}/\text{CuO}@CA_{0.2}$  shown in Fig. 2(d) is associated with the stretching

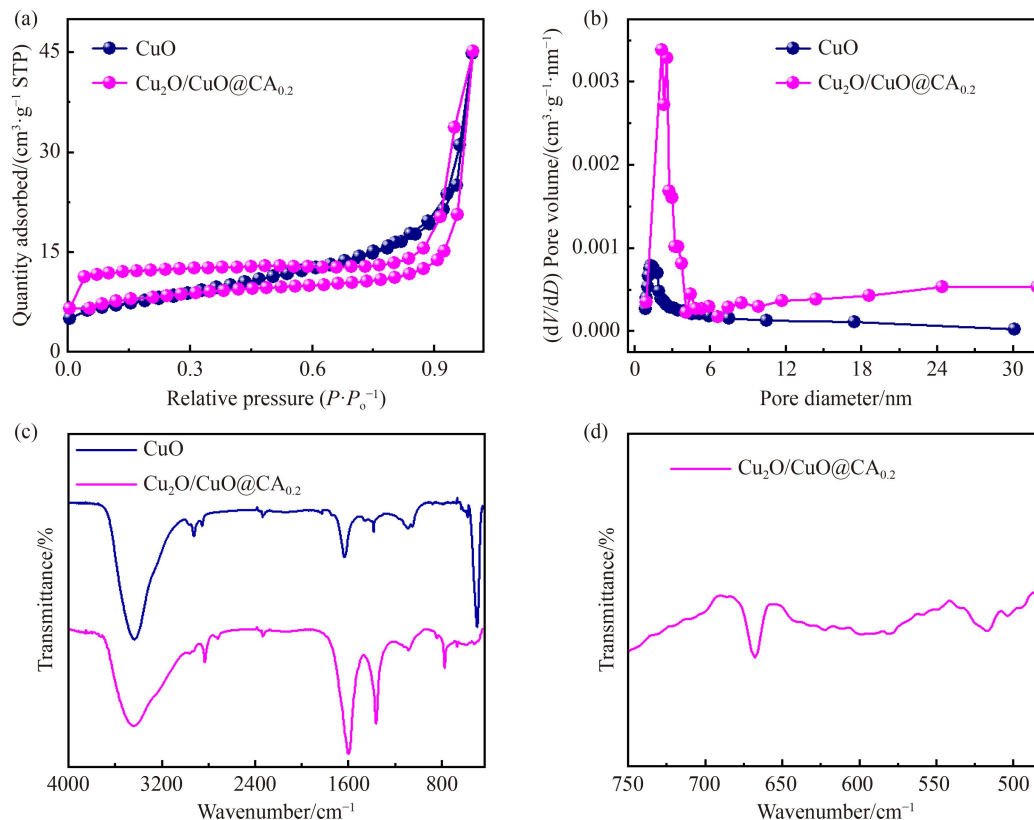


**Fig. 2** (a)  $N_2$  adsorption–desorption isotherms and (b) Barret–Joyner–Halenda pore size distributions of copper oxide (CuO) and  $Cu_2O/CuO@CA_{0.2}$ ; (c) Fourier transform infrared (FTIR) spectra of CuO and  $Cu_2O/CuO@CA_{0.2}$  and (d) its local zoom of FTIR spectrum for  $Cu_2O/CuO@CA_{0.2}$ .

vibration of Cu–O in  $Cu_2O$ , while the peak at  $521\text{ cm}^{-1}$  is attributed to the stretching vibration of Cu–O in CuO. This result further indicated the successful preparation of  $Cu_2O/CuO@CA_{0.2}$ .

To further verify the successful fabrication of the  $Cu_2O/CuO@CA_{0.2}$ , X-ray diffraction (XRD) characterizations of CuO and  $Cu_2O/CuO@CA_{0.2}$  were performed. In addition, the elemental composition and chemical states of  $Cu_2O/CuO@CA_{0.2}$  were investigated using X-ray photoelectron spectroscopy (XPS). The XRD and XPS results are shown in Fig. 3. In Fig. 3(a), the typical diffraction peaks of CuO can be observed (PDF#44-0706-CuO). With regards to the  $Cu_2O/CuO@CA_{0.2}$ , the diffraction peaks at  $35.4^\circ$  and  $38.3^\circ$  correspond to the (110) and (111) crystallographic planes of CuO, respectively, and those at  $36.3^\circ$ ,  $42.3^\circ$ ,  $61.4^\circ$  and  $73.5^\circ$  correspond to the (111), (200), (220) and (311) crystallographic planes of  $Cu_2O$  (PDF#77-0199), respectively. Thus, the results indicate that partial  $Cu_2O$  was formed during CuO calcination. The composite formed by the two compounds was interpenetrated into the carbon nanosheets of the carbon aerogels, which is consistent with the FTIR and SEM results.

In the survey spectrum of  $Cu_2O/CuO@CA_{0.2}$  shown in Fig. 3(b), the binding energy peaks for C, N, O and Cu can be observed. In the C 1s spectrum shown in Fig. 3(c),

three diffraction peaks located at 284.8, 285.7 and 290.3 eV can be attributed to C–C, O–C and O=C bonding, respectively [43]. The peaks at 399.5 and 401.6 eV in the N 1s spectrum correspond to  $NH_2/N-C$  and  $NH_3^+$ , respectively (Fig. 3(d)). The high-resolution O 1s spectrum was fitted into three peaks, identified as O–Cu (531.1 eV), O=C (532.8 eV) and H–O (534.7 eV) (Fig. 3(e)) [44]. The presence of  $Cu^{2+}$  was confirmed by the peaks of Cu  $2p_{3/2}$  and Cu  $2p_{1/2}$  at 933.4 and 953.2 eV, respectively, in the Cu 2p spectrum. The presence of  $Cu^+$  was confirmed by the peaks at 932.0 and 951.8 eV, indicating  $Cu_2O$  formation [43]. The aforementioned results are consistent with those of SEM, FTIR and XRD, indicating the successful preparation of  $Cu_2O/CuO@CA_{0.2}$ .

Figure 4 shows the Mott–Schottky, ultraviolet photoelectron spectroscopy (UPS), photocurrent response and electrochemical impedance spectroscopy (EIS) results of CuO and  $Cu_2O/CuO@CA_{0.2}$ . The energy band structure of semiconductors is closely related to their redox properties, which essentially determine their charge separation efficiency. To elucidate the energy band structure of  $Cu_2O/CuO@CA_{0.2}$ , Mott–Schottky plots were constructed and UPS measurements were performed. As shown in Figs. 4(a) and 4(b), the positive slope of the Mott–Schottky curves indicated that both CuO and  $Cu_2O$ /

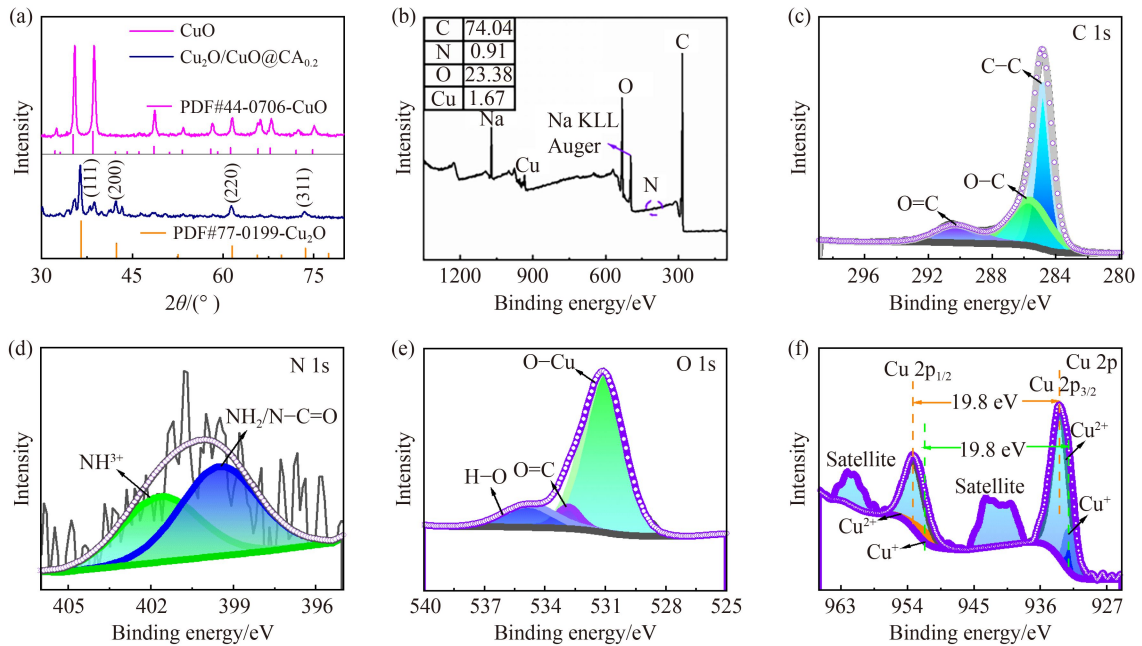


**Fig. 3** (a) X-ray diffraction patterns of copper oxide and  $\text{Cu}_2\text{O}/\text{CuO}@CA_{0.2}$ ; X-ray photoelectron spectroscopy (XPS) spectra of  $\text{Cu}_2\text{O}/\text{CuO}@CA_{0.2}$ : (b) XPS survey spectrum, (c) C 1s, (d) N 1s, (e) O 1s and (f) Cu 2p.

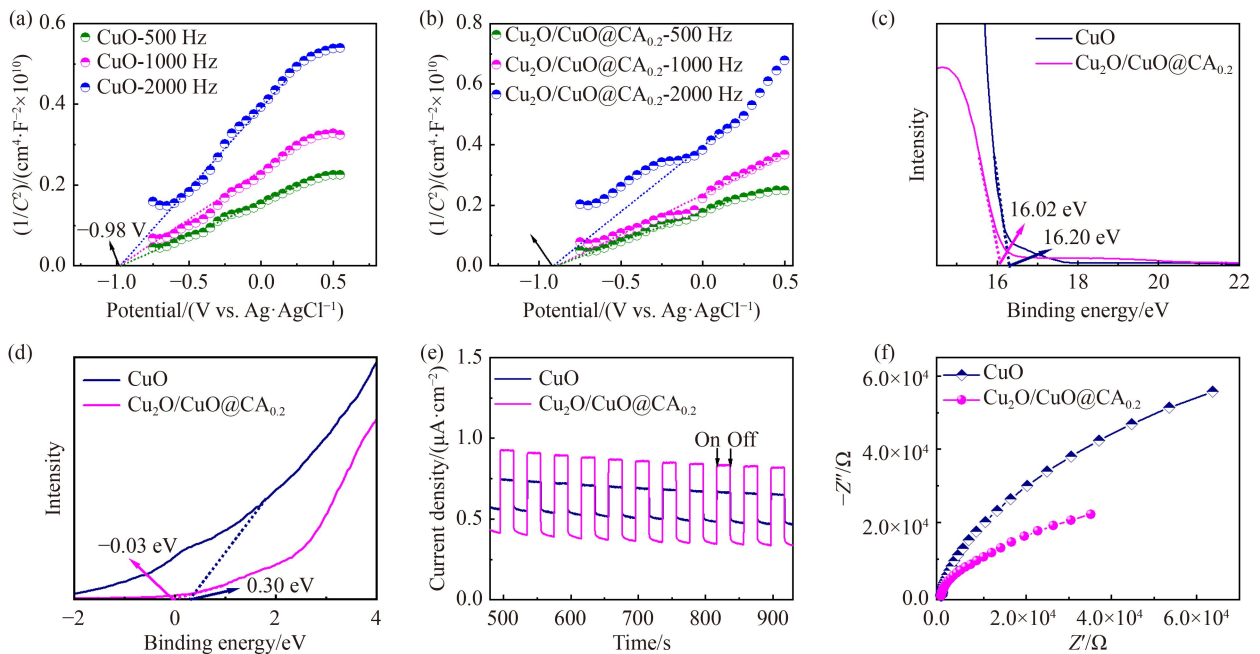


**Fig. 4** Mott-Schottky plots of (a) copper oxide (CuO) and (b)  $\text{Cu}_2\text{O}/\text{CuO}@CA_{0.2}$ ; (c, d) ultraviolet photoelectron spectroscopy of CuO and  $\text{Cu}_2\text{O}/\text{CuO}@CA_{0.2}$ ; (e) periodic ON/OFF photocurrent response of CuO and  $\text{Cu}_2\text{O}/\text{CuO}@CA_{0.2}$  in  $0.1 \text{ mol}\cdot\text{L}^{-1} \text{ Na}_2\text{SO}_4$  electrolyte under visible light irradiation ( $\lambda > 420 \text{ nm}$ ) at  $0.5 \text{ V vs. Ag}/\text{AgCl}$  electrode; (f) electrochemical impedance spectroscopy Nyquist plots in the visible light illumination of CuO and  $\text{Cu}_2\text{O}/\text{CuO}@CA_{0.2}$ .

$\text{CuO}@CA_{0.2}$  are n-type semiconductors. Based on the horizontal intercepts obtained from the maximum slope, the flat-band potentials of CuO and  $\text{Cu}_2\text{O}/\text{CuO}@CA_{0.2}$  were  $-0.98$  and  $-0.90 \text{ V}$ , respectively. The conduction band of the n-type semiconductor is  $0.2 \text{ V}$  more negative than the flat-band potential [45]. Thus, the conduction bands of CuO and  $\text{Cu}_2\text{O}/\text{CuO}@CA_{0.2}$  were  $-0.78$  and

$-0.7 \text{ V vs. Ag}/\text{AgCl}$ , respectively. The conversion of the reference electrode of the conduction band to a normal hydrogen electrode (NHE) was achieved using the Nernst formula ( $E_{\text{NHE}} = E_{\text{Ag}/\text{AgCl}} + 0.197$  and  $\text{pH} = 7$ ), and the calculated conduction bands for CuO and  $\text{Cu}_2\text{O}/\text{CuO}@CA_{0.2}$  were calculated as  $-0.98$  and  $-0.90 \text{ V}$ , respectively. In addition, UPS was used to study the electronic states

and valence band (VB) of the photocatalysts. Figures 4(c) and 4(d) show the UPS results of CuO and Cu<sub>2</sub>O/CuO@CA<sub>0.2</sub>, respectively. The work function ( $\Phi$ ) was first calculated according to  $\Phi = 21.20 - E_{\text{cutoff}}$ , where 21.20 is the UV excitation energy, and  $E_{\text{cutoff}}$  was derived from the point of intersection at high binding energy.  $E_{\text{cutoff}}$  values for CuO and Cu<sub>2</sub>O/CuO@CA<sub>0.2</sub> were 16.20 and 16.02 eV, respectively. The  $\Phi$  values of CuO and Cu<sub>2</sub>O/CuO@CA<sub>0.2</sub> were calculated using its formula as 5.00 and 5.18 eV, respectively. The VB positions were calculated based on  $E_{\text{VB}} (\text{vs. vacuum}) = \Phi + E_{\text{edge}}$ , where  $E_{\text{edge}}$  is the intersection point at low binding energy.  $E_{\text{edge}}$  values for CuO and Cu<sub>2</sub>O/CuO@CA<sub>0.2</sub> were 0.30 and -0.03 eV, and the calculated  $E_{\text{VB}} (\text{vs. vacuum})$  values were 0.86 and 0.71 eV, respectively. Finally, the reference was transformed into NHE using the equation:  $E_{\text{VB}} (\text{vs. NHE}) = E_{\text{VB}} (\text{vs. vacuum}) - 4.44$ . The VBs of CuO and Cu<sub>2</sub>O/CuO@CA<sub>0.2</sub> vs. NHE were calculated to be 0.86 and 0.71 V, respectively. According to the Mott–Schottky and UPS results, the bandgaps of CuO and Cu<sub>2</sub>O/CuO@CA<sub>0.2</sub> were calculated to be 1.84 and 1.61 eV, respectively. The

charge separation of CuO and Cu<sub>2</sub>O/CuO@CA<sub>0.2</sub> was investigated by recording transient photocurrent curves. As shown in Fig. 4(e), Cu<sub>2</sub>O/CuO@CA<sub>0.2</sub> exhibits a higher photocurrent response than CuO, indicating that Cu<sub>2</sub>O/CuO@CA<sub>0.2</sub> has a higher photogenerated charge separation ability. Moreover, the EIS results showed that the arc radius of Cu<sub>2</sub>O/CuO@CA<sub>0.2</sub> is smaller than that of CuO (Fig. 4(f)), indicating that the charge transfer resistance of Cu<sub>2</sub>O/CuO@CA<sub>0.2</sub> is significantly lower, allowing for the efficient separation and migration of photoinduced excitons [46].

### 3.2 Photocatalytic activity tests

To increase methylene blue degradation, experiments were conducted to determine the optimal process conditions. The results are shown in Fig. 5. The pH value affects the photocatalyst surface properties, such as the surface charge and dissociation of contaminants [47]. Meanwhile, methylene blue is a cationic dye; an alkaline system is beneficial for its degradation. In this work, the

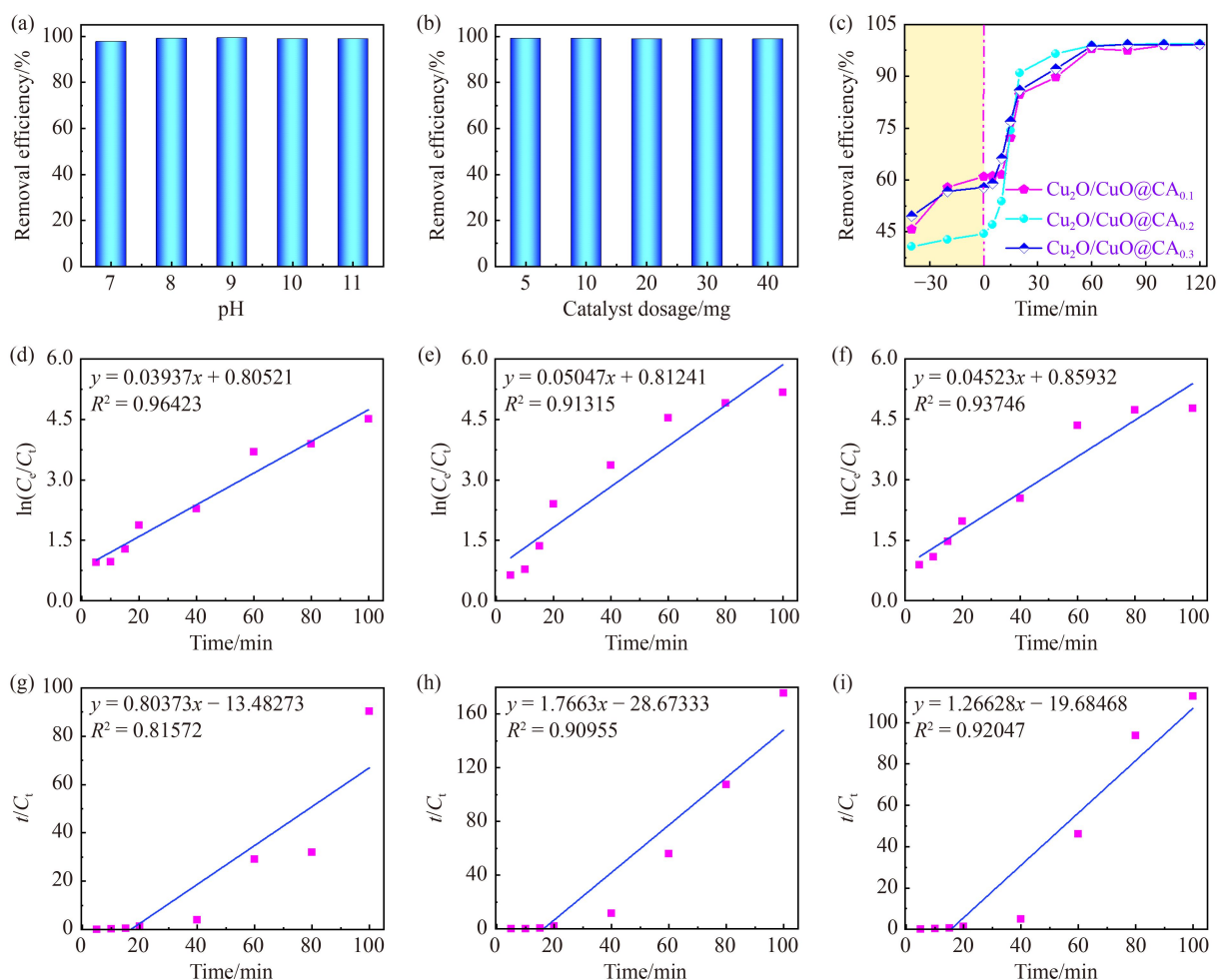


**Fig. 5** The effects of (a) pH and (b) catalyst dosage on the photocatalytic degradation of methylene blue using Cu<sub>2</sub>O/CuO@CA<sub>0.2</sub>; the effect of (c) reaction time on the photocatalytic degradation of methylene blue using Cu<sub>2</sub>O/CuO@CA<sub>x</sub>; photocatalytic degradation kinetics of methylene blue using (d, g) Cu<sub>2</sub>O/CuO@CA<sub>0.1</sub>, (e, h) Cu<sub>2</sub>O/CuO@CA<sub>0.2</sub> and (f, i) Cu<sub>2</sub>O/CuO@CA<sub>0.3</sub>.

photocatalytic degradation methylene blue activity was monitored by measuring the absorbance of the solution at different pH values (7, 8, 9, 10 and 11). Initially,  $\text{Cu}_2\text{O}/\text{CuO}@CA_{0.2}$  (10 mg) was added to a methylene blue solution (10 mL and 100 ppm) and reacted in the dark with magnetic stirring for 40 min to reach adsorption/desorption equilibrium, followed by irradiation for 60 min. As shown in Fig. 5(a), the degradation rate of methylene blue reached 99.08% when pH increased to 8. The degradation of methylene blue remained constant upon further increasing the pH values. Therefore, pH = 8 was selected as the best pH value from the perspective of green chemistry.

Next, the amount of catalyst significantly impacts the degradation efficiency and oxidation capacity. Here, a series of experiments were performed with different  $\text{Cu}_2\text{O}/\text{CuO}@CA_{0.2}$  dosages for the photocatalytic degradation of methylene blue. As shown in Fig. 5(b), the degradation rate of methylene blue reached 99.09% when the  $\text{Cu}_2\text{O}/\text{CuO}@CA_{0.2}$  dosage was 5 mg. However, the degradation rate of methylene blue slightly decreased upon increasing the amount of  $\text{Cu}_2\text{O}/\text{CuO}@CA_{0.2}$ . This phenomenon can be attributed to the increased turbidity of the nanoparticles, which causes more scattering effects and less visible light penetration [2].

A series of tests were performed to investigate the effect of CuO addition in  $\text{CuO}/\text{CuO}@CA_x$  on the degradation of methylene blue. Similarly, the experiments were first treated in dark conditions for 40 min to reach adsorption/desorption equilibrium. Afterwards, the reactions were carried out under the irradiation with 300 W Xenon lamp. Obviously, all samples displayed excellent photocatalytic degradation performance (Fig. 5(c)). Among them,  $\text{Cu}_2\text{O}/\text{CuO}@CA_{0.2}$  exhibited the best photocatalytic performance, with the degradation rate of methylene blue reaching 90.98% when irradiated for 20 min, which was higher than those of  $\text{CuO}/\text{CuO}@CA_{0.1}$  and  $\text{CuO}/\text{CuO}@CA_{0.3}$  systems. In the following, the effects of reaction times on their photocatalytic degradation efficiencies of methylene blue were studied. As shown in Fig. 5(c), the degradation rate of methylene blue was significantly increased upon exposure to a 300 W xenon lamp irradiation for 20 min, showing a linear trend. A slight increase in degradation efficiency was observed between 20 and 60 min. However, it was almost constant between 60 and 120 min due to the gradual occupation of the active catalyst sites as the reaction proceeded, which reduced the efficiency of the system [2]. Among the tested photocatalysts,  $\text{Cu}_2\text{O}/\text{CuO}@CA_{0.2}$  exhibited the highest photocatalytic degradation efficiency, degrading  $\geq 90\%$  of methylene blue in 60 min. To further demonstrate the performance of the photocatalysts, kinetic curve fitting was performed. Figures 5(d)–5(i) fitting results revealed that the degradation process followed first-order reaction kinetics. In addition, as shown in Figs. 5(d)–5(f), the rate constant of  $\text{Cu}_2\text{O}/\text{CuO}@$

$CA_{0.2}$  was determined to be 0.05047, which is higher than those of  $\text{Cu}_2\text{O}/\text{CuO}@CA_{0.1}$  (0.03937) and  $\text{Cu}_2\text{O}/\text{CuO}@CA_{0.3}$  (0.04523), indicating that  $\text{Cu}_2\text{O}/\text{CuO}@CA_{0.2}$  demonstrated the best photocatalytic degradation performance.

To investigate the effect of photo corrosion on the photocatalyst, the content of copper ions released from  $\text{Cu}_2\text{O}/\text{CuO}@CA_{0.2}$  after the reaction was also explored. Here, 5 mg of  $\text{Cu}_2\text{O}/\text{CuO}@CA_{0.2}$  was added to 10 mL of methylene blue solution with a concentration of 100 ppm (the copper content was  $54.75 \text{ mg}\cdot\text{L}^{-1}$ ), and the mixed system was stirred for 40 min under dark conditions and then irradiated by visible light for 60 min. After that, the contents of copper ions were detected by inductively coupled plasma mass spectrometry, and  $0.1919 \text{ mg}\cdot\text{L}^{-1}$  of copper ions was observed, indicating that the  $\text{Cu}_2\text{O}/\text{CuO}@CA_{0.2}$  has an excellent stability.

To better understand the photocatalytic efficiency of  $\text{Cu}_2\text{O}/\text{CuO}@CA_{0.2}$ , the efficiency of  $\text{Cu}_2\text{O}/\text{CuO}@CA_{0.2}$  and the reported catalysts on the photocatalytic degradation of methylene blue were investigated. Obviously, the  $\text{Cu}_2\text{O}/\text{CuO}@CA_{0.2}$  has excellent photocatalytic activity in the methylene blue degradation as compared with the reported catalysts (Table S1, cf. Electronic Supplementary Material) [26–29,33,48]. As for the  $\text{MgFe}_2\text{O}_4/\text{CuO}/\text{GO}$ , the reaction time is lower than that of this work (Table S1, entries 1 and 2). However, the initial concentration of methylene blue in the  $\text{Cu}_2\text{O}/\text{CuO}@CA_{0.2}$  ( $100 \text{ mg}\cdot\text{L}^{-1}$ ) photocatalytic system is higher than that of  $\text{MgFe}_2\text{O}_4/\text{CuO}/\text{GO}$  ( $10 \text{ mg}\cdot\text{L}^{-1}$ ). Meanwhile, the  $\text{MgFe}_2\text{O}_4/\text{CuO}/\text{GO}$  has large preparation costs and tedious preparation processes when compared with  $\text{Cu}_2\text{O}/\text{CuO}@CA_{0.2}$ . Overall, this photocatalytic system shows excellent photocatalytic performance and has a promising application in the treatment of methylene blue.

### 3.3 ESR characterization and poisoning experiments

To investigate the photocatalytic degradation mechanism of methylene blue using  $\text{Cu}_2\text{O}/\text{CuO}@CA_{0.2}$ , ESR trapping experiments were conducted. The results are shown in Fig. 6. The electrons ( $e^-$ ), holes ( $h^+$ ), superoxide radical ( $\cdot\text{O}_2^-$ ), hydroxyl radical ( $\cdot\text{OH}$ ) and singlet oxygen ( $^1\text{O}_2$ ) signals of  $\text{Cu}_2\text{O}/\text{CuO}@CA_{0.2}$  were detected in the absence of catalysts in the dark and upon exposure to catalysts for 5 and 10 min. Initially, 2,2,6,6-tetramethylpiperidine-*N*-oxide (TEMPO) was used to detect  $e^-$  and  $h^+$ . As shown in Fig. 6(a), a stable triplet peak with a 1:1:1 intensity was generated using TEMPO (in the absence of a catalyst or in the dark with a catalyst). After 5 min of irradiation, TEMPO was converted, and the corresponding peak intensity decreased, indicating the production of  $e^-$ . When irradiated for 10 min, the peak intensity was further reduced, indicating more  $e^-$  were generated. The signal intensity trends of  $h^+$  were similar to those of  $e^-$  (Fig. 6(b)) owing to the pair formation of  $e^-$  and  $h^+$ .

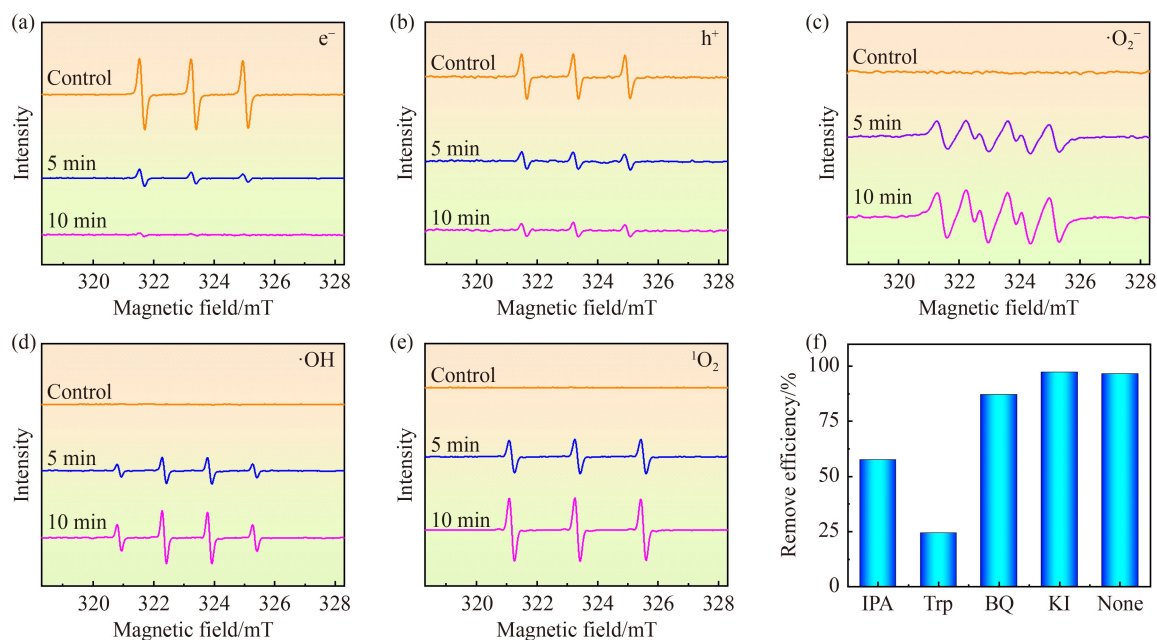


**Fig. 6** 2,2,6,6-Tetramethylpiperidine-*N*-oxide electron spin resonance (ESR) spin labeling for (a) electrons and (b) holes, 5,5-dimethyl-1-pyrroline-*N*-oxide ESR spin trapping for (c) superoxide radical and (d) hydroxyl radical as well as 2,2,6,6-tetramethyl-4-piperidone-1-yloxy ESR spin labeling for (e) singlet oxygen (control: under the dark conditions or irradiation without samples); (f) the effect of different active oxidation species on methylene blue's degradation.

Furthermore, 5,5-dimethyl-1-pyrroline-*N*-oxide (DMPO) was used to monitor the generated  $\cdot\text{O}_2^-$  and  $\cdot\text{OH}$  during the photocatalytic degradation processes. In Fig. 6(c),  $\cdot\text{O}_2^-$  signals were not detectable in the absence of catalysts when irradiated using visible light or in the darkness with photocatalysts, indicating that visible light is necessary for producing  $\cdot\text{O}_2^-$ . Under visible light irradiation, the signals of DMPO/ $\cdot\text{O}_2^-$  with an intensity of 1:1:1:1 were detected in the  $\text{Cu}_2\text{O}/\text{CuO}@CA_{0.2}$  system, indicating that  $\cdot\text{O}_2^-$  was generated. Similarly, the signal intensity of DMPO/ $\cdot\text{O}_2^-$  increased with the irradiation time, suggesting more  $\cdot\text{O}_2^-$  was produced. For  $\cdot\text{OH}$ , all the trends were similar to those of  $\cdot\text{O}_2^-$ , except for the DMPO/ $\cdot\text{OH}$  intensity of 1:2:2:1 (Fig. 6(d)).

$^1\text{O}_2$  is also a typical oxidatively active species, with 2,2,6,6-tetramethyl-4-piperidone-1-yloxy commonly used as a trapping agent in ESR measurements to investigate the production of  $^1\text{O}_2$ . As displayed in Fig. 6(e), no signals were observed in the system without  $\text{Cu}_2\text{O}/\text{CuO}@CA_{0.2}$  irradiated by visible light or in darkness. However, a triplet peak with an intensity of 1:1:1 was generated when visible light was irradiated on the  $\text{Cu}_2\text{O}/\text{CuO}@CA_{0.2}$  system. The corresponding signal intensity increased with a longer exposure time to light, indicating the production of  $^1\text{O}_2$  and its contents increasing with irradiation time.

To determine the effects of the main active species produced by the  $\text{Cu}_2\text{O}/\text{CuO}@CA_{0.2}$  photocatalytic system for the degradation of methylene blue, a series of poisoning experiments were performed over  $\text{Cu}_2\text{O}/\text{CuO}@CA_{0.2}$  under optimal conditions (5 mg  $\text{Cu}_2\text{O}/\text{CuO}@CA_{0.2}$ ,

pH = 8, 100 ppm of methylene blue solution and exposure to the dark for 40 min and visible light irradiation for 60 min). The effects of  $\cdot\text{OH}$ ,  $^1\text{O}_2$ ,  $\cdot\text{O}_2^-$  and  $h^+$  on the photocatalytic degradation of methylene blue were investigated using isopropyl alcohol, tryptophan, *p*-benzoquinone and potassium iodide as sacrificial agents. As shown in Fig. 6(f), adding *p*-benzoquinone, isopropyl alcohol and tryptophan inhibited the photocatalytic degradation of methylene blue compared to the  $\text{Cu}_2\text{O}/\text{CuO}@CA_{0.2}$  photocatalytic system without a sacrificial agent. Moreover, compared with the other two sacrificial agents, the addition of tryptophan resulted in the lowest degradation rate of methylene blue, indicating that  $^1\text{O}_2$  was the main active species involved in the photocatalytic degradation of methylene blue. However, after adding potassium iodide, the degradation rate of methylene blue was slightly enhanced, indicating that the  $h^+$  inhibited the degradation of methylene blue.

#### 3.4 Possible mechanism of photocatalytic degradation of methylene blue via $\text{Cu}_2\text{O}/\text{CuO}@CA_{0.2}$

Based on previously reported data and the results of ESR spectroscopy measurements as well as poisoning experiments, a possible reaction pathway for the photocatalytic degradation of methylene blue using  $\text{Cu}_2\text{O}/\text{CuO}@CA_{0.2}$  was proposed [49]. Initially, the different potentials of the VBs and conduction bands of CuO and  $\text{Cu}_2\text{O}$  result in the transfer of photogenerated  $e^-$  and  $h^+$  between CuO and  $\text{Cu}_2\text{O}$ . In case of visible light irradiation,  $e^-$  is transferred from  $\text{Cu}_2\text{O}$  to CuO, while  $h^+$  is transferred from CuO to

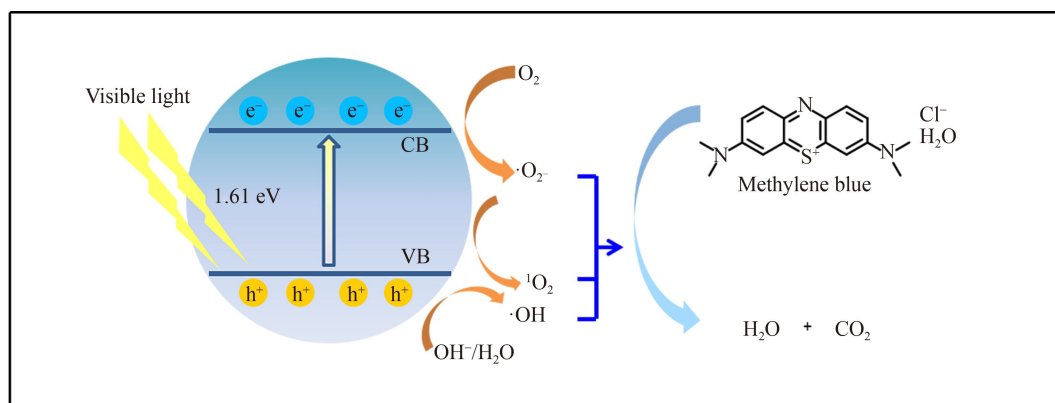
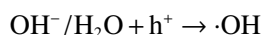
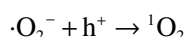
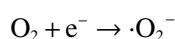


Fig. 7 The possible photocatalytic mechanism for degradation of methylene blue using  $\text{Cu}_2\text{O}/\text{CuO}@CA_{0.2}$ .

$\text{Cu}_2\text{O}$  [50]. Furthermore, carbon aerogels have excellent conductivity and superior charge carrier mobility, resulting in enhanced charge separation. The pathways for the generation of active oxidation species are postulated as follows:



The excited  $e^-$  reacts with the  $\text{O}_2$  adsorbed on the catalyst surface to form  $\cdot\text{O}_2^-$ , as shown in Fig. 7. Some of the  $\cdot\text{O}_2^-$  further reacts with  $h^+$  to form  ${}^1\text{O}_2$ . Moreover,  $h^+$  can combine with  $\text{OH}^-$  and  $\text{H}_2\text{O}$  to form  $\cdot\text{OH}$ . Eventually, methylene blue adsorbed on the catalyst surface was degraded to  $\text{CO}_2$  and  $\text{H}_2\text{O}$  under their comprehensive effects.

## 4 Conclusions

In summary,  $\text{Cu}_2\text{O}/\text{CuO}@CA_{0.2}$  with a vertically aligned layered structure was successfully prepared via a freeze-drying-calcination method.  $\text{Cu}_2\text{O}/\text{CuO}@CA_{0.2}$  exhibited a narrower bandgap and faster photogenerated carrier separation/migration than  $\text{CuO}$ . According to the first-order kinetics equation, photocatalytic experiments demonstrated that  $\text{Cu}_2\text{O}/\text{CuO}@CA_{0.2}$  displays excellent photocatalytic degradation of methylene blue. The optimised reaction conditions yielded an optimal degradation rate of 99.09% in 60 min ( $\text{Cu}_2\text{O}/\text{CuO}@CA_{0.2}$  dosage: 5 mg, pH 8 and methylene blue solution concentration: 100 ppm). The usage of free radical scavengers and tracking probes revealed that  ${}^1\text{O}_2$  is the main active oxidation species involved in the degradation process. Therefore, this study proposed a simple, effective and controllable method for preparing biomass-based photocatalysts loaded with metal oxides to facilitate the application of photocatalytic technology in the field of environmental protection.

**Acknowledgements** This work was supported by the Foundation of National Natural Science Foundation of China (Grant No. 22008018), NSFC-CONICFT Joint Project (Grant No. 51961125207), China Postdoctoral Science Foundation (Grant No. 2020M670716), Liaoning Province “Xingliao Talent Plan” Outstanding Talent Project (Grant No. XL YC1901004), Innovation Support Program for High-level Talents of Dalian (Top and Leading Talents) (Grant No. 201913), the Foundation of Guangxi Key Laboratory of Clean Pulp & Papermaking and Pollution Control, College of Light Industry and Food Engineering, Guangxi University (Grant No. 2021KF08), Dalian City Outstanding Talent Project (Grant No. 2019RD13), Start-up Fund for Doctoral Research of Dalian Polytechnic University (Grant No. 2020-07), the Foundation of State Key Laboratory of Biobased Material and Green Papermaking (Grant No. KF201914), Qilu University of Technology, Shandong Academy of Sciences, and the Foundation of Key Laboratory of State Forestry and Grassland Administration for Plant Fiber Functional Materials (Grant No. 2020KFJJ06). We also thank the Shiyanjia laboratory for the XPS analysis.

**Electronic Supplementary Material** Supplementary material is available in the online version of this article at <https://doi.org/10.1007/s11705-023-2305-0> and is accessible for authorized users.

## References

- Gusain R, Gupta K, Joshi P, Khatri O P. Adsorptive removal and photocatalytic degradation of organic pollutants using metal oxides and their composites: a comprehensive review. *Advances in Colloid and Interface Science*, 2019, 272: 102009
- Ebrahimi R, Maleki A, Zandsalimi Y, Ghanbari R, Shahmoradi B, Rezaee R, Safari M, Joo S W, Daraei H, Harikaranahalli Puttaiah S, Giahi O. Photocatalytic degradation of organic dyes using  $\text{WO}_3$ -doped  $\text{ZnO}$  nanoparticles fixed on a glass surface in aqueous solution. *Journal of Industrial and Engineering Chemistry*, 2019, 73: 297–305
- de Oliveira Guidolin T, Possolli N M, Polla M B, Wermuth T B, Franco de Oliveira T, Eller S, Klegues Montedo O R, Arcaro S, Cechinel M A P. Photocatalytic pathway on the degradation of methylene blue from aqueous solutions using magnetite nanoparticles. *Journal of Cleaner Production*, 2021, 318: 128556
- Sahu S, Pahi S, Sahu J K, Sahu U K, Patel R K. Kendu (diospyros melanoxylon Roxb) fruit peel activated carbon—an efficient bioadsorbent for methylene blue dye: equilibrium, kinetic, and thermodynamic study. *Environmental Science and Pollution*

- Research International, 2020, 27(18): 22579–22592
- Borghei Y S, Hosseini M, Ganjali M R. Visual detection of miRNA using peroxidase-like catalytic activity of DNA-CuNCs and methylene blue as indicator. *Clinica Chimica Acta*, 2018, 483: 119–125
  - Lu G, Nagbanshi M, Goldau N, Mendes Jorge M, Meissner P, Jahn A, Mockenhaupt F P, Müller O. Efficacy and safety of methylene blue in the treatment of malaria: a systematic review. *BMC Medicine*, 2018, 16(1): 59
  - Hosseini H, Zirakjou A, McClements D J, Goodarzi V, Chen W H. Removal of methylene blue from wastewater using ternary nanocomposite aerogel systems: carboxymethyl cellulose grafted by polyacrylic acid and decorated with graphene oxide. *Journal of Hazardous Materials*, 2022, 421: 126752
  - Ren L F, Tang Z, Du J Y, Chen L, Qiang T T. Recyclable polyurethane foam loaded with carboxymethyl chitosan for adsorption of methylene blue. *Journal of Hazardous Materials*, 2021, 417: 126130
  - Li L X, Lv Y, Wang J, Jia C, Zhan Z S, Dong Z L, Liu L L, Zhu X D. Enhance pore structure of cyanobacteria-based porous carbon by polypropylene to improve adsorption capacity of methylene blue. *Bioresource Technology*, 2022, 343: 126101
  - Sharma R, Saini H, Paul D R, Chaudhary S, Nehra S P. Removal of organic dyes from wastewater using *Eichhornia crassipes*: a potential phytoremediation option. *Environmental Science and Pollution Research International*, 2021, 28(6): 7116–7122
  - Giwa A R A, Bello I A, Olabintan A B, Bello O S, Saleh T A. Kinetic and thermodynamic studies of fenton oxidative decolorization of methylene blue. *Heliyon*, 2020, 6(8): e04454
  - Jiang F H, Cao D F, Hu S X, Wang Y, Zhang Y, Huang X H, Zhao H, Wu C N, Li J G, Ding Y L, Liu K. High-pressure carbon dioxide-hydrothermal enhance yield and methylene blue adsorption performance of banana pseudo-stem activated carbon. *Bioresource Technology*, 2022, 354: 127137
  - Benhouria A, Islam M A, Zaghouane-Boudiaf H, Boutahala M, Hameed B H. Calcium alginate-bentonite-activated carbon composite beads as highly effective adsorbent for methylene blue. *Chemical Engineering Journal*, 2015, 270: 621–630
  - Zhao R, Li Y Z, Sun B L, Chao S, Li X, Wang C, Zhu G S. Highly flexible magnesium silicate nanofibrous membranes for effective removal of methylene blue from aqueous solution. *Chemical Engineering Journal*, 2019, 359: 1603–1616
  - Bedekar P A, Kshirsagar S D, Gholave A R, Govindwar S P. Degradation and detoxification of methylene blue dye adsorbed on water hyacinth in semi continuous anaerobic-aerobic bioreactors by novel microbial consortium-SB. *RSC Advances*, 2015, 5(120): 99228–99239
  - Ong S A, Toorisaka E, Hirata M, Hano T. Treatment of methylene blue-containing wastewater using microorganisms supported on granular activated carbon under packed column operation. *Environmental Chemistry Letters*, 2007, 5(2): 95–99
  - Liu K N, Ma J L, Yang X P, Jin D N, Li Y C, Jiao G J, Yao S Q, Sun S L, Sun R C. Boosting electron kinetics of anatase TiO<sub>2</sub> with carbon nanosheet for efficient photo-reforming of xylose into biomass-derived organic acids. *Journal of Alloys and Compounds*, 2022, 906: 164276
  - Zhao H Q, Zhu Q, Zhuang Y, Zhan P, Qi Y O, Ren W Q, Si Z H, Cai D, Yu S S, Qin P Y. Hierarchical ZnIn<sub>2</sub>S<sub>4</sub> microspheres as photocatalyst for boosting the selective biohydrogenation of furfural into furfuryl alcohol under visible light irradiation. *Green Chemical Engineering*, 2022, 3(4): 385–394
  - Liu Z D, Liu K N, Sun R C, Ma J L. Biorefinery-assisted ultra-high hydrogen evolution via metal-free black phosphorus sensitized carbon nitride photocatalysis. *Chemical Engineering Journal*, 2022, 446: 137128
  - Yang R G, Fu Y M, Wang H N, Zhang D P, Zhou Z, Cheng Y Z, Meng X, He Y O, Su Z M. ZIF-8/covalent organic framework for enhanced CO<sub>2</sub> photocatalytic reduction in gas–solid system. *Chemical Engineering Journal*, 2022, 450: 138040
  - Wang T Q, Tian B B, Han B, Ma D R, Sun M Z, Hanif A, Xia D H, Shang J. Recent advances on porous materials for synergetic adsorption and photocatalysis. *Energy and Environmental Materials*, 2022, 5(3): 711–730
  - Balbuena J, Carraro G, Cruz M, Gasparotto A, Maccato C, Pastor A, Sada C, Barreca D, Sánchez L. Advances in photocatalytic NO<sub>x</sub> abatement through the use of Fe<sub>2</sub>O<sub>3</sub>/TiO<sub>2</sub> nanocomposites. *RSC Advances*, 2016, 6(78): 74878–74885
  - Li J K, Lv C P, Liu X H, Jiao Z B, Liu N. Highly durable Ag-CuO heterostructure-decorated mesh for efficient oil/water separation and *in situ* photocatalytic dye degradation. *Energy and Environmental Materials*, 2021, 4(4): 611–619
  - Masudy-Panah S, Zhuk S, Tan H R, Gong X, Dalapati G K. Palladium nanostructure incorporated cupric oxide thin film with strong optical absorption, compatible charge collection and low recombination loss for low cost solar cell applications. *Nano Energy*, 2018, 46: 158–167
  - Dai Y H, Wang Y, Liu B, Yang Y H. Metallic nanocatalysis: an accelerating seamless integration with nanotechnology. *Small*, 2015, 11(3): 268–289
  - Raees A, Jamal M A, Ahmed I, Silanpaa M, Saad Algarni T. Synthesis and characterization of CeO<sub>2</sub>/CuO nanocomposites for photocatalytic degradation of methylene blue in visible light. *Coatings*, 2021, 11(3): 305
  - Bayat F, Sheibani S. Enhancement of photocatalytic activity of CuO-Cu<sub>2</sub>O heterostructures through the controlled content of Cu<sub>2</sub>O. *Materials Research Bulletin*, 2022, 145: 111561
  - Ma J G, Tian Z J, Li L, Lu Y, Xu X L, Hou J W. Loading nano-CuO on TiO<sub>2</sub> nanomeshes towards efficient photodegradation of methylene blue. *Catalysts*, 2022, 12(4): 383
  - Nuengmatcha P, Porrawatkul P, Chanthai S, Sricharoen P, Limchoowong N. Enhanced photocatalytic degradation of methylene blue using Fe<sub>2</sub>O<sub>3</sub>/graphene/CuO nanocomposites under visible light. *Journal of Environmental Chemical Engineering*, 2019, 7(6): 103438
  - Toe C Y, Scott J, Amal R, Ng Y H. Recent advances in suppressing the photocorrosion of cuprous oxide for photocatalytic and photoelectrochemical energy conversion. *Journal of Photochemistry and Photobiology C: Photochemistry Reviews*, 2019, 40: 191–211
  - Jiang D H, Xue J B, Wu L Q, Zhou W, Zhang Y G, Li X H. Photocatalytic performance enhancement of CuO/Cu<sub>2</sub>O heterostructures for photodegradation of organic dyes: effects of

- CuO morphology. *Applied Catalysis B: Environmental*, 2017, 211: 199–204
32. Ge J L, Zhang Y F, Park S J. Recent advances in carbonaceous photocatalysts with enhanced photocatalytic performances: a mini review. *Materials*, 2019, 12(12): 1916
  33. Waheed I F, Al-Janabi O Y T, Foot P J S. Novel  $\text{MgFe}_2\text{O}_4$ -CuO/GO heterojunction magnetic nanocomposite: synthesis, characterization, and batch photocatalytic degradation of methylene blue dye. *Journal of Molecular Liquids*, 2022, 357: 119084
  34. He B, Feng M, Chen X Y, Zhao D W, Sun J. One-pot construction of chitin-derived carbon/g- $\text{C}_3\text{N}_4$  heterojunction for the improvement of visible-light photocatalysis. *Applied Surface Science*, 2020, 527: 146737
  35. Zhang L X, Wang C L, Jiu H F, Xu Q W, Li X, Song W, Luo S Y, Zhao J H. Metal-organic framework derived carbon-encapsulated hollow CuO/ $\text{Cu}_2\text{O}$  heterostructure heterohedron as an efficient electrocatalyst for hydrogen evolution reaction. *Dalton Transactions*, 2022, 51(8): 3349–3356
  36. Rangarajan G, Jayaseelan A, Farnood R. Photocatalytic reactive oxygen species generation and their mechanisms of action in pollutant removal with biochar supported photocatalysts: a review. *Journal of Cleaner Production*, 2022, 346: 131155
  37. Shan Y W, Guo Y, Wang Y, Du X R, Yu J, Luo H, Wu H, Boury B, Xiao H, Huang L L, Chen L. Nanocellulose-derived carbon/g- $\text{C}_3\text{N}_4$  heterojunction with a hybrid electron transfer pathway for highly photocatalytic hydrogen peroxide production. *Journal of Colloid and Interface Science*, 2021, 599: 507–518
  38. Yang W, Yang W, Zou R, Huang Y F, Lai H H, Chen Z H, Peng X W. Cellulose nanofiber-derived carbon aerogel for advanced room-temperature sodium-sulfur batteries. *Carbon Energy*, 2022, 5(1): e203
  39. Wang L, Wu Q, Zhao B Z, Li Z L, Zhang Y H, Huang L, Yu S T. Multi-functionalized carbon aerogels derived from chitosan. *Journal of Colloid and Interface Science*, 2022, 605: 790–802
  40. Peydayesh M, Vogt J, Chen X L, Zhou J T, Donat F, Bagnani M, Müller C R, Mezzenga R. Amyloid-based carbon aerogels for water purification. *Chemical Engineering Journal*, 2022, 449: 137703
  41. Jiao G J, Ma J L, Zhang J Q, Zhou J H, Sun R C. High-efficiency capture and removal of phosphate from wastewater by 3D hierarchical functional biomass-derived carbon aerogel. *Science of the Total Environment*, 2022, 827: 154343
  42. Zhao X L, Tan Y X, Wu F C, Niu H Y, Tang Z, Cai Y Q, Giesy J P. Cu/ $\text{Cu}_2\text{O}$ /CuO loaded on the carbon layer derived from novel precursors with amazing catalytic performance. *Science of the Total Environment*, 2016, 571: 380–387
  43. Bai W D, Wu M B, Du X L, Gong W L, Ding Y H, Song C H, Liu L. Synergistic effect of multiple-phase rGO/CuO/ $\text{Cu}_2\text{O}$  heterostructures for boosting photocatalytic activity and durability. *Applied Surface Science*, 2021, 544: 148607
  44. Dubale A A, Ahmed I N, Zhang Y J, Yang X L, Xie M H. A facile strategy for fabricating C@ $\text{Cu}_2\text{O}$ /CuO composite for efficient photochemical hydrogen production with high external quantum efficiency. *Applied Surface Science*, 2020, 534: 147582
  45. Gao X C, Feng J, Su D W, Ma Y C, Wang G X, Ma H Y, Zhang J T. *In-situ* exfoliation of porous carbon nitride nanosheets for enhanced hydrogen evolution. *Nano Energy*, 2019, 59: 598–609
  46. Xu Y S, Fan M J, Yang W J, Xiao Y H, Zeng L T, Wu X, Xu Q H, Su C L, He Q J. Homogeneous carbon/potassium-incorporation strategy for synthesizing red polymeric carbon nitride capable of near-infrared photocatalytic  $\text{H}_2$  production. *Advanced Materials*, 2021, 33(39): 2101455
  47. Toloman D, Popa A, Stan M, Stefan M, Vlad G, Ulinici S, Baisan G, Silipas T D, Macavei S, Leostean C, Pruneanu S, Pogacean F, Suciuc R C, Barbu-Tudoran L, Pana O. Visible-light-driven photocatalytic degradation of different organic pollutants using Cu doped ZnO-MWCNT nanocomposites. *Journal of Alloys and Compounds*, 2021, 866: 159010
  48. Sathiyavimal S, Vasantharaj S, Kaliannan T, Pugazhendhi A. Eco-biocompatibility of chitosan coated biosynthesized copper oxide nanocomposite for enhanced industrial (azo) dye removal from aqueous solution and antibacterial properties. *Carbohydrate Polymers*, 2020, 241: 116243
  49. Serrà A, Gómez E, Michler J, Philippe L. Facile cost-effective fabrication of Cu@ $\text{Cu}_2\text{O}$ @CuO-microalgae photocatalyst with enhanced visible light degradation of tetracycline. *Chemical Engineering Journal*, 2021, 413: 127477
  50. Zhang W W, Chen X, Zhao X T, Yin M Y, Feng L P, Wang H. Simultaneous nitrogen doping and  $\text{Cu}_2\text{O}$  oxidization by one-step plasma treatment toward nitrogen-doped  $\text{Cu}_2\text{O}$ @CuO heterostructure: an efficient photocatalyst for  $\text{H}_2\text{O}_2$  evolution under visible light. *Applied Surface Science*, 2020, 527: 146908